Journal of Alloys and Compounds 509 (2011) 7447–7457

Contents lists available at ScienceDirect

Journal of Alloys and Compounds

journal homepage: www.elsevier.com/locate/jallcom

Structural properties and electrical resistivity of Na-substituted lanthanum manganites: $La_{1-x}Na_xMnO_{3+y}$ ($x = 0.1$, 0.125 and 0.15)

Dinesh Varshney*, Neha Dodiya, Mohammed Wasim Shaikh

School of Physics, Vigyan Bhavan, Devi Ahilya University, Khandwa Road Campus, Indore 452001, India

ARTICLE INFO

Article history:
Received 4 February 2011
Received in revised form 8 April 2011
Accepted 11 April 2011
Available online 22 April 2011

Keywords:
Manganites
Structural properties
Electronic transport
Metal–insulator transitions
Phonon–electron interaction and Polarons

ABSTRACT

The structural properties and electrical resistivity of the polycrystalline $La_{1-x}Na_xMnO_{3+y}$ ($x = 0.1$, 0.125 and 0.15) are investigated. The result of the Rietveld refinement of X-ray powder diffraction following the FullProf refinement program indicates that these compounds having a rhombohedrally distorted structure with space group $R\bar{3}C$. Both the lattice parameter and unit-cell volume decreases with increased Na content. There is a systematic change in both the Mn–O–Mn bond angle and the tolerance factor with Na content. The temperature dependence of resistivity shows that all samples undergo a metal–insulator transition at well-defined transition temperature T_{mi}. The metallic resistivity for temperatures $T < T_{mi}$, is theoretically analysed with electron–phonon, electron–electron and electron–magnon scattering. For temperatures, $T > T_{mi}$, the semiconducting nature is discussed with small polaron conduction (SPC) model. The resistivity shows an upturn at low temperatures that has been explained by considering both the enhanced electron–electron interactions attributed to Coulomb interaction (CI) between carriers and the Kondo-like spin dependent scattering.

1. Introduction

The rich diversity of the physical properties of doped $LaMnO_3$ manganites ($La_{1-x}A_xMnO_3$, where A = divalent alkaline-earth metal ion) has generated amazing interest in manganites. The metal–insulator transition observed near the Curie temperature results colossal magnetoresistance (CMR) as defined in terms of sharp decrease of the electric resistance of manganites under external magnetic field [1,2]. The CMR materials have been focused due to many fold reasons: the comprehension of basic phenomena related to the CMR effect, the optimization of known compounds, and synthesis of new materials with the aim of enhancing and tuning their physical properties [3,4].

La ion may be replaced not only by divalent alkaline-earth metal ions but also by monovalent alkali metals. Compounds synthesized by partial substitution of lanthanum by monovalent alkali metals such as Na^+, K^+, Rb^+ were reported long back [5] and was tested as oxidation catalysts for exhaust gases for internal combustion engines. Renewed interest in these materials came up due to their magnetoresistive and magnetocaloric properties [6–8]. Although most of the studies were focused on the divalent cation-doped $La_{1-x}A_xMnO_3$ compounds, investigations on monovalent cation doping as Na, K, and Ag are limited.

The parent compound, $LaMnO_3$, is an antiferromagnetic insulator (AFI) characterized by a super exchange coupling between Mn^{3+} sites facilitated by a single e_g electron subjected to strong correlation effects. Substitution on La^{3+} ion by a divalent or a monovalent ion results in a mixed valence states of Mn ($Mn^{3+}$and Mn^{4+}), where Mn^{4+} lacks e_g electron, and hence the itinerant hole associated with Mn^{4+} ion may hop to Mn^{3+}. The hopping is favorable only when the localized spins of these ions are parallel and this is the essence of double exchange (DE) mechanism [9] and is expected to explain the ferromagnetic metallic nature of manganites below metal–insulator transition, T_{mi}. Millis et al. [10] stressed that the physics of manganites is dominated by the interplay between a strong electron–phonon coupling e.g. via Jahn–Teller effects and large Hund's coupling effect that optimizes the electronic kinetic energy by the formation of ferromagnetic phase. However, it has been found that factors such as the average size of the cations, vacancies at La and Mn-sites and the oxygen stoichiometry also plays a crucial role in electrical and magnetic properties of manganite materials [11–14]. The key query is that are the monovalent-doped manganites fulfill the criterions set for divalent-doped manganites.

The electrical resistivity of doped manganites as a function of temperature exhibits three regimes (a) low temperature metallic like conduction with an unexpectedly large absolute value of the resistivity, (b) an abrupt drop in resistivity associated with magnetic ordering, and (c) high-temperature activated conduction. Analysis of charge transport in the ferromagnetic metallic

---

* Corresponding author. Tel.: +91 7312465689; fax: +91 7312465689.
E-mail address: vdinesh33@rediffmail.com (D. Varshney).

0925-8388/$ – see front matter © 2011 Elsevier B.V. All rights reserved.
doi:10.1016/j.jallcom.2011.04.075

state is essential in clarifying the specific mechanisms responsible for the resistivity behavior. Electron–phonon, electron–electron, electron–magnon scattering and polaronic effects are the major proponents of various conceptions in electrical transport.

In the case of Na (monovalent) doping, for every amount x of Na, an amount $2x$ of Mn^{3+} will be converted to Mn^{4+}. As a result, even a small amount of Na doping results in a large number of charge carriers and a consequent increase in the conductivity is achieved. Moreover, because of the large valency difference between Na^+ and La^{3+}, there is an increased difference in potential between the Na and the La sites although the ionic radii of La^{3+} and Na^+ are comparable. Hence one expects that study of the effect of Na doping in the manganites system will enable a better understanding of the CMR effect in these compounds to be achieved.

With these motivations, in the present work we have investigated in detail the property-structural relationship of $La_{1-x}Na_xMnO_{3+y}$ ($x = 0.1$, 0.125, 0.15) manganites prepared by solid-state ceramic route technique to seek the role of substitution effects (monovalent cation Na^+ for trivalent La^{3+}) on the structural and magnetic properties following X-ray diffraction (XRD), energy dispersive X-ray analysis (EDAX), scanning electron microscopy (SEM), and *dc* electrical resistivity.

The present investigations are organized as follows. The experimental details are given in the next section. Later on, we supply technical details to estimate the electron–phonon, electron–electron and electron–magnon scattering contribution to resistivity for metallic region ($T < T_{mi}$), polaron conduction for semiconducting resistivity ($T > T_{mi}$) and motivate them by simple physical arguments before summarizing our results. We employ the Bloch–Gruneisen method to estimate the independent contributions of acoustic and optical phonons. For semi conducting region we compute resistivity behavior with small polaron conduction (SPC). The small polaron model takes care of coherent motion of charge carriers and involves a relaxation due to a low-lying optical phonon mode. A summary and our main conclusions are presented in the last section.

The main findings for $La_{1-x}Na_xMnO_{3+y}$ ($x = 0.1$, 0.125 and 0.15) manganites include: (i) the Rietveld refinement of room temperature XRD data confirms that all the samples are crystallize in rhombohedrally distorted structure with space group $R\,\bar{3}C$ without any other secondary or impurity phase, (ii) the lattice parameters and unit-cell volume decrease with increasing Na concentration. On the other hand, both the Mn–O–Mn bond angle and the tolerance factor show an increasing trend with increasing Na content, (iii) the EDAX results confirm purity and chemical composition of these compounds. The SEM results reveal that compositions are homogeneous and the particle sizes are in the range of 2–4 μm, (iv) temperature dependence of the resistivity at zero magnetic fields of all the samples exhibit metallic behavior at low temperatures ($T < T_{mi}$) and semiconductor-like features above transition temperature T_{mi}. The value of T_{mi} increases from ~253 K to ~282 K as the Na content increases from 0.1 to 0.15. The magnitude of the resistivity in the entire temperature range decreases with increasing Na concentration in the samples. At very low temperatures (~30 K), the resistivity of all the samples shows upturn with decrease in temperature, (v) the classical electron–phonon model of resistivity, for example, the Bloch–Gruneisen (BG) model retraces the reported metallic resistivity behavior in the temperature range ($T < T_m$), (vi) the quadratic temperature (T^2) dependence of ρ_{diff} [$=\rho_{\text{exp}} - (\rho_0 + \rho_{\text{e–ph}})$] is interpreted in terms of 3D electron–electron inelastic scattering and is essential for the description of resistivity, (vii) the $T^{4.5}$ temperature dependence of ρ_{diff} [$=\rho_{\text{exp}} - (\rho_0 + \rho_{\text{e–ph}} + \rho_{\text{e–e}})$] accounting for electron–magnon interactions is also essential for the correct description of resistivity, (viii) the $La_{1-x}Na_xMnO_{3+y}$ ($x = 0.1$, 0.125 and 0.15) is a good metal in the temperature region $T < T_{mi}$ and Mott–Ioffe–Regel criterion for metallic conductivity is valid, $k_F l \sim 1$, $\varepsilon_F \tau > 1$, and (ix) the small polaron conduction model consistently explains the higher temperature resistivity behavior ($T > T_{mi}$).

Table 1
EDAX results for $La_{1-x}Na_xMnO_{3+y}$ ($x = 0.1$, 0.125 and 0.15) samples.

Element present	Atomic percentages		
	$x = 0.1$	$x = 0.125$	$x = 0.15$
La	13.86	13.92	14.74
Na	2.33	2.41	2.82
Mn	16.70	16.17	16.10
O	67.11	67.50	66.34

2. Experimental detail

2.1. Synthesis of samples

We synthesized a series of sodium-substituted lanthanum manganites having the general formula, $La_{1-x}Na_xMnO_{3+y}$ ($x = 0.1$, 0.125, 0.15) by conventional solid-state reaction method. The advantage of solid-state reaction method for synthesizing oxide materials over other synthesis methods is many fold. Foremost is the readily availability of starting materials, suitability for the preparation of high purity, degree of homogenization achieved on mixing, intimacy of contact between the grains and accurately stoichiometric compounds by optimizing the processing and synthesis parameters that have a large influence on the properties of final products. Mixture of stoichiometric amount of La_2O_3, Na_2CO_3, and MnO_2 was calcined (at 900 °C) in air for 24 h with two intermediate grindings and then sintered (at 950 °C) for 48 h after being pelletized. The pellets were finally annealed at 1000 °C in oxygen atmosphere for 12 h. Low reaction temperature and long firing times have been chosen to get a single-phase compound without losing much Na during the synthesis procedure.

2.2. Characterization

2.2.1. X-ray diffraction (XRD)

The powder X-ray patterns were recorded using a Rigaku Diffractometer with Cu $K\alpha$ radiation. A scanning rate of $0.01^\circ\,s^{-1}$ was adopted and the data were taken at room temperature in the 2θ range of 10–90°. Monochromatic X-rays of $\lambda = 1.5406$ Å $K_{\alpha 1}$ line generating by 40 kV and 100 mA power settings from a Cu target were made to fall on the prepared samples. The diffraction pattern was obtained by varying the scattering angle 2θ from 10° to 90° in step size of 0.01°. XRD data were refined by means of the Rietveld method using the FullProf refinement program [15].

2.2.2. Scanning electron microscopy (SEM) and energy-dispersive X-ray analysis (EDAX)

High-resolution scanning electron microscopy (SEM) and energy-dispersive X-ray analysis (EDAX) have been done using an INSA Oxford instrument model no. JEOL – JSM 5600 with 3.5 nm resolution, ×18 to 300,000 (in 136 steps) magnification and 0.5–30 kV (53 steps) accelerating voltage.

2.2.3. Iodometric titration

The ratio of the Mn^{3+}/Mn^{4+} concentration and oxygen content of the samples was determined by iodometric titration. Typically, about 100 mg of the sample was dissolved in 10 ml of 1:10 HCl containing about 1 g of solid KI. Liberated iodine was titrated against standard sodium thiosulphate (0.04 N) solution using starch as an indicator.

2.2.4. dc electrical resistivity

Electrical resistivity measurements were carried out by standard four-probe method in the temperature range 5–300 K. Electrical contacts were made using Indium on a rectangular rod of the sample. We have used a Stanford Research Systems lock-in amplifier (model SR 850) and commercial Lakeshore controllers (model DCR93CA).

3. Results and discussion

In order to ascertain the Na content in these samples, EDAX measurement was carried out. These measurements confirmed the cationic compositions of the samples. EDAX plots for $La_{1-x}Na_xMnO_{3+y}$ ($x = 0.1$, 0.125, 0.15) samples are shown in Fig. 1 and the results of the analysis are largely summarized in Table 1. No trace of any impurity was found, indicating the purity of the samples. It is also clear that there is no loss of any ingredient after sintering. The EDAX results suggest that the precursors have fully

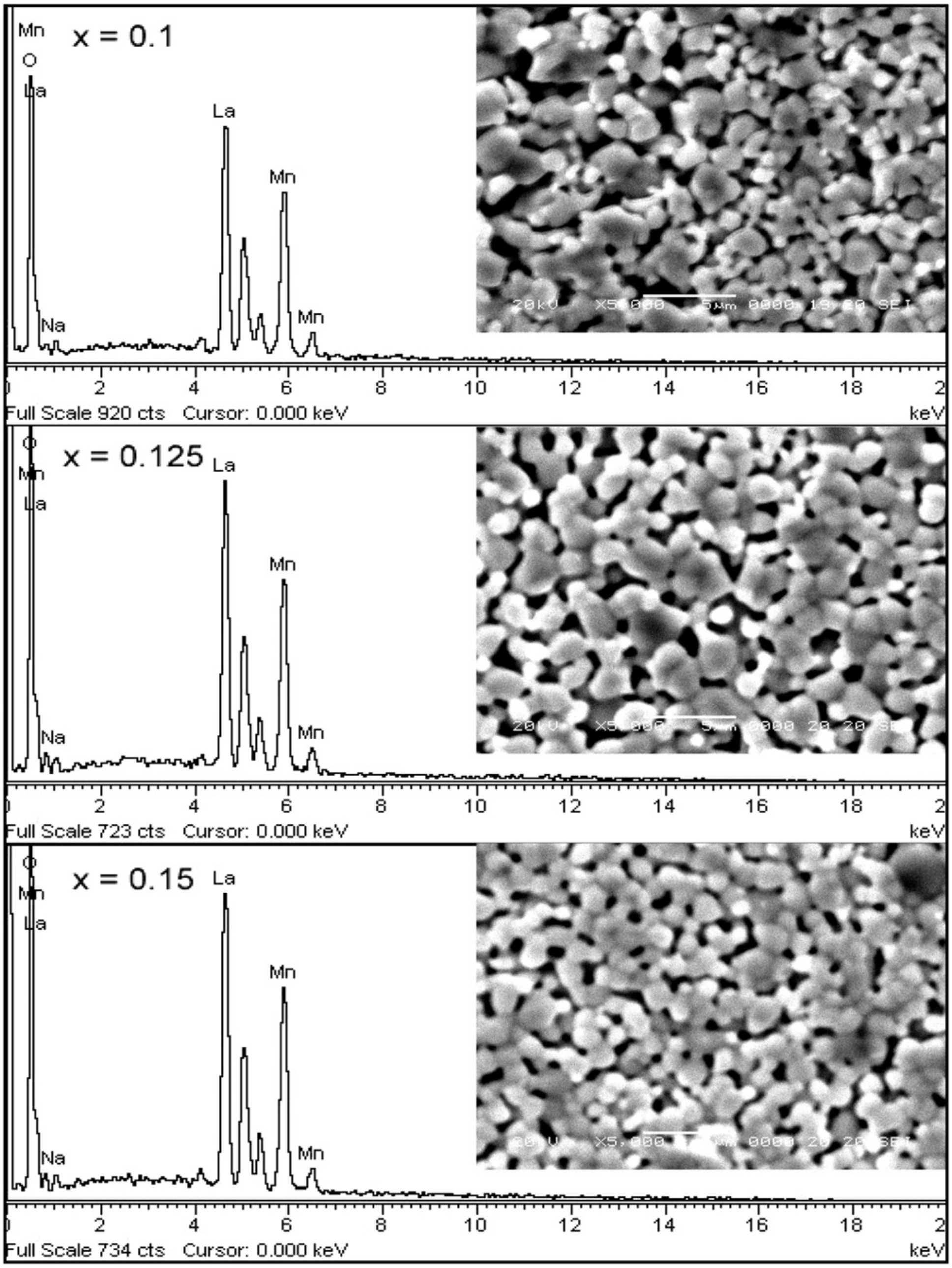

Fig. 1. EDAX plots for $La_{1-x}Na_xMnO_{3+y}$ (x = 0.1, 0.125, 0.15) samples. The insets are the scanning electron micrographs.

undergone the chemical reaction to form the expected perovskite material. The reason for EDAX characterization was to ratify the purity and surety of the chemical composition. Scanning electron micrographs of all the samples are also shown in the inset of Fig. 1. The micrograph of samples shows voluminous and porous morphology and the particle sizes are in the range of 2–4 μm. The SEM results reveal that compositions are homogeneous. We note that the samples were prepared by solid-state reaction method; the oxygen deficiency cannot be ruled out. Thus, for other characterization as resistivity the samples were annealed in oxygen at 1000 °C for 12 h. If it is assumed that, La and Na are present in all the samples in there respective stoichiometric ratio and Mn is present in a mixed valence state ($Mn^{3+}$and Mn^{4+}), then the chemical formula of the compounds can be written as: $La^{3+}{}_{1-x}Na^{+}{}_{x}Mn^{3+}{}_{1-\Delta}Mn^{4+}{}_{\Delta}O_{3+y}$ (x = 0.1, 0.125, 0.15), where $y = (\Delta/2) - x$. The value of Δ and hence the oxygen content (y) of the samples was determined by iodometric titration method. Typically, about 100 mg of the sample was dissolved in 10 ml of 1:10 HCl containing about 1 g of solid KI. The following reactions occur:

$$2Mn^{3+} + 2Cl^{-} \rightarrow Cl_2 + 2Mn^{2+},$$

$$Mn^{4+} + 2Cl^{-} \rightarrow Cl_2 + Mn^{2+},$$

$$Cl_2 + 2I^{-} \rightarrow 2Cl^{-} + I_2.$$

Liberated iodine was titrated against standard sodium thiosulphate (0.04 N) solution using starch as an indicator. The value of Δ can be determined by using the volume V of sodium thiosulphate solution used in titration as:

$$\Delta = \frac{(M - 16x)NV - m}{m - 8NV},$$

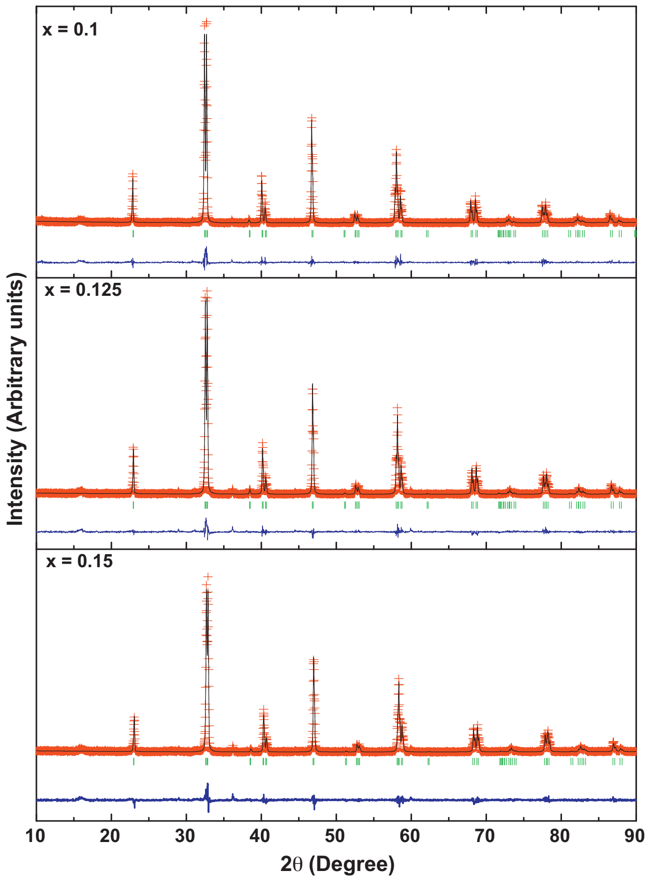

Fig. 2. XRD pattern of $La_{1-x}Na_xMnO_{3+y}$ ($x = 0.1, 0.125, 0.15$) with Rietveld refinement.

where *m* is the mass, *M* is the molecular weight of the sample and *N* is the normality of the standard sodium thiosulphate solution.

The calculated values of Mn^{4+}/Mn^{3+} ratio and oxygen content *y* are illustrated in Table 2. It is noticed that the ratio increases with increased doping concentration also the oxygen content is sufficient in all the samples. We must mention that the oxygen stoichiometry is purely based on the mixed oxidation state of Mn and hence the amount of the doping concentration *x*. It plays a crucial role in electrical and magnetic properties of manganite materials.

The room temperature powder XRD pattern of all the samples along with Rietveld refinement is shown in Fig. 2. The crosses show the actual data and the calculated curve is superimposed on them. The bottom line shows the difference between the experimental and the calculated XRD patterns. Bragg peaks appear as vertical lines. Very good agreement between the calculated and the observed data is obtained which confirms that the samples are prepared without any other secondary or impurity phase. XRD patterns of the samples can be indexed by rhombohedral lattice (Hexagonal setting) with space group $R\,\bar{3}C$. The structural parameters are listed in Table 2 along with the values of the goodness-of-fit factor *s*, the residual factor *Rp* and the weighted residual factor *Rwp*. These values are in close agreement with published results [16].

It can be seen that the lattice parameters decrease from $a = 5.5118$ Å to 5.4944 Å and $c = 13.3378$ Å to 13.3264 Å with increasing Na concentration. A similar feature is observed for the unit-cell volume as shown in Table 2, indicating that the lattice shrinks and the unit cell becomes smaller with increasing Na concentration. This can be correlated with the increase in Mn^{4+} content with doping, which is smaller (ionic radii, 0.53 Å) than the Mn^{3+} ion (ionic radii, 0.645 Å) [17]. The presence of smaller cations in the B sublattice of the ABO_3 perovskite is responsible for the reduction in unit cell volume. It is well known that one of possible origins of the lattice distortion of perovskite-based structures is the deformation of the $Mn^{3+}O_6$ octahedra originating from the JT effect that is inherent to the high-spin ($S = 2$) Mn^{3+} ions with double degeneracy of the e_g orbital. Obviously, this kind of distortion is directly related to the concentration of Mn^{3+} ions.

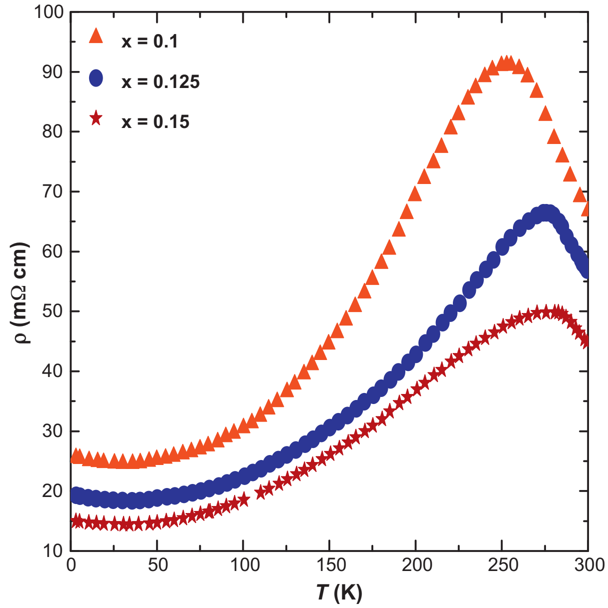

Fig. 3. Temperature dependence of the resistivity for $La_{1-x}Na_xMnO_{3+y}$ ($x = 0.1, 0.125$ and 0.15) between 5 and 300 K.

Another possible origin of the lattice distortion is the average ionic radius of the A-site element, which is governed by the tolerance factor $t = (r_A + r_O)/\sqrt{2}(r_{Mn} + r_O)$ (where r_A, r_{Mn}, and r_O, are the ionic radii for A-site, Mn-site and Oxygen ion, respectively). As *t* is close to 1, the cubic perovskite structure is realized. Furthermore, if r_A decreases, *t* also does, the lattice structure transforms to the rhombohedral ($0.96 < t < 1$) and then to the orthorhombic structure ($t < 0.96$), in which the bending of Mn–O–Mn bond and the deviating of the bond angle from 180° increase.

For $La_{1-x}Na_xMnO_{3+y}$ samples, the ionic size of Na^{1+} (∼1.390 Å) is slightly larger than that of La^{3+} (1.360 Å) [17], which results in the tolerance factor *t* is larger than 0.96 as illustrated in Table 2. On increasing Na content, both the Mn–O–Mn bond angle and the tolerance factor show an increasing trend, resulting in the crystal structure transforms to cubic-like symmetry. Based on the structural results of Na-doping systems, it is inferred that the structure symmetry of doped perovskite manganese oxides is affected by the size of doped ions.

Fig. 3 shows the temperature dependence of the resistivity at zero magnetic fields for $La_{1-x}Na_xMnO_3$ with $0.1 \geq x \geq 0.15$ between 5 and 300 K. All the samples exhibit metallic behavior ($\partial\rho/\partial T < 0$) at low temperatures ($T < T_{mi}$) and semiconductor-like features above T_{mi}. The value of T_{mi} increases from ∼253 K to ∼282 K as the Na content increases from 0.1 to 0.15. The magnitude of the resistivity in the entire temperature range decreases with increasing Na concentration in the samples. In case of monovalent Na doping, for every amount of *x* of Na, an amount 2*x* of Mn^{3+} will get converted to Mn^{4+}. As a result, even a small amount of Na doping results in a large number of charge carriers in the e_g band and results in decrease in the resistivity. However, at very low temperatures (∼30 K), the resistivity of all the samples shows upturn with decrease in temperature which is consistent with the earlier reports [18–21].

Table 2
Structure data from X-ray powder diffraction studies of $La_{1-x}Na_xMnO_{3+y}$ ($x = 0.1, 0.125, 0.15$). The atoms are located at the following Wyckoff positions for $R\bar{3}C$ space group (hexagonal setting), La, Na, 6(a): (0, 0, 1/4); Mn 6(b): (0, 0, 0); O 18(e): (X, 0, 1/4). The bond lengths correspond to each unit cell. R_p, R_{wp}, and S are the residual factor, the weighted residual factor, and the goodness-of-fit factor respectively.

	Composition		
X	0.1	0.125	0.15
Lattice parameters			
a (Å)	5.5118	5.5058	5.4944
c (Å)	13.3378	13.3354	13.3264
V (Å^3)	350.92	350.09	348.40
Bond distances			
La/Na–O	2.4731	2.4721	2.4650
Mn–O	1.9614	1.9603	1.9552
Bond angle			
Mn–O–Mn (°)	163.42	163.45	163.46
Positional parameter of oxygen			
X	0.5513	0.5543	0.5512
Tolerance factor			
T	0.966	0.969	0.972
Residual factors			
R_p	15.9	15.4	17.7
R_{wp}	21.9	21.2	24.0
R_{exp}	17.5	17.1	20.0
Goodness of fit			
S	1.51	1.54	1.44
Ratio of manganese ions			
Mn^{4+}/Mn^{3+}	0.27	0.36	0.46
Oxygen content			
Y	0.0076	0.0081	0.0083

With a view to understand the conduction mechanism of monovalent Na doped lanthanum manganites, in metallic region ($T < T_{mi}$), we employ the Bloch–Gruneisen (BG) method to estimate the independent contributions of acoustic and optical phonons. We start with the general expression for the temperature dependent part of the resistivity, following the Debye model, which is given by [22]

$$\rho(T) \approx \left(\frac{3}{\hbar e^2 v_F^2}\right) \frac{k_B T}{M v_s^2} \int_0^{2k_F} \left|F(q)\right|^2 \left[\frac{x q^3 \ dq}{[e^x - 1][1 - e^{-x}]}\right], \tag{1}$$

with $x = \hbar\omega/k_B T$. In the above, $F(q)$ is the Fourier transform of the potential associated with one lattice site, v_F being the Fermi velocity. v_s being the sound velocity. Eq. (1) in terms of acoustic phonon contribution yields the Bloch–Gruneisen function of temperature dependence resistivity:

$$\rho_{ac}(T, \theta_D) = 4A_{ac} T \left(\frac{T}{\theta_D}\right)^4 \int_0^{\theta_D/T} x^5 (e^x - 1)^{-1} (1 - e^{-x})^{-1} \, dx, \tag{2}$$

where A_{ac} is a constant of proportionality defined as

$$A_{ac} \cong \frac{3\pi^2 e^2 k_B}{k_F^2 v_s^2 L \hbar v_F^2 M}. \tag{3}$$

On the other hand, in case of the Einstein type of phonon spectrum (an optical mode) $\rho_{op}(T)$ may be described as follows:

$$\rho_{op}(T, \theta_E) = A_{op} {\theta_E}^2 T^{-1} [e^{\theta_E/T} - 1]^{-1} [1 - e^{-\theta_E/T}]^{-1}. \tag{4}$$

A_{op} is defined analogously to equation (3). Thus, the phonon resistivity can be conveniently modeled by combining both terms arising from acoustic and optical phonons

$$\rho_{e-ph}(T) = \rho_{ac}(T, \theta_D) + \rho_{op}(T, \theta_E). \tag{5}$$

If the Matthiessen rule is obeyed, the resistivity may be represented as a sum $\rho\ (T) = \rho_0 + \rho_{e-ph}(T)$, where ρ_0 is the residual resistivity that does not depend on temperature as electrons also scatter off impurities, defects and disordered regions. Finally, the total resistivity is now rewritten as

$$\begin{aligned} \rho(T, \theta_D, \theta_E) = \rho + \rho_{ac}(T, \theta_D) + \rho_{op}(T, \theta_E) = \rho_0 \\ + 4A_{ac}\left(\frac{T}{\theta_D}\right)^4 T \times \int_0^{\theta_D/T} x^5 (e^x - 1)^{-1} (1 - e^{-x})^{-1} \ dx \\ + A_{op} \theta_E^2 T^{-1} \left[\exp\left(\frac{\theta_E}{T}\right) - 1\right]^{-1} \left[1 - \exp\left(-\frac{\theta_E}{T}\right)\right]^{-1}. \end{aligned} \tag{6}$$

For the temperature dependent resistivity analysis one needs the value of Debye (Einstein) temperature and has been estimated using an effective interionic interaction potential (EIoIP) with the long-range Coulomb, van der Waals (vdW) interaction and the short-range repulsive interaction up to second neighbour ions within the Hafemeister and Flygare approach. Details of this calculation, including the assumptions made for estimation of Debye (Einstein) temperature of the system, are given in the Appendix.

Initially, we have calculated the values of the model parameters (range b and hardness ρ) for a pair such as Mn–O and La/Na–O and have the total of the $La_{1-x}Na_xMnO_{3+y}$ (Table 3). Using these model parameters, we have evaluated the values of the second order elastic constants (SOECs) which are illustrated in Table 3. Finally we evaluate the values of acoustic and optical phonon frequency (ω_D, ω_{LO} and ω_{TO}) corresponding to Debye and Einstein temperature. The computed values of ω_D, ω_{LO} and ω_{TO} are pre-

Table 3
The model parameters (b, ρ) and the second order elastic constants for $La_{1-x}Na_xMnO_{3+y}$ ($x = 0.1, 0.125, 0.15$) samples.

x	Model parameters				Second order elastic constants		
	b_1 (La/Na–O) (10^{-12} erg)	ρ_1 (La/Na–O) (Å)	b_2 (Mn–O) (10^{-12} erg)	ρ_2 (Mn–O) (Å)	C_{11} (Dyne cm^{-2})	C_{12} (Dyne cm^{-2})	C_{44} (Dyne cm^{-2})
0.1	0.623	0.32	3.245	0.369	7.399	3.542	2.417
0.125	1.051	0.331	4.429	0.347	8.593	4.795	3.505
0.15	1.152	0.332	5.434	0.336	9.69	6.077	4.623

Table 4
Parameters obtained corresponding to the best fit to the experimental data of $La_{1-x}Na_xMnO_3$ samples by using BG model.

x	T_{mi} (K)	ω_D (meV)	ω_{LO} (meV)	ω_{TO} (meV)	Parameters obtained from BG model		
					ρ_0 (mΩ cm)	$A_{ac} \times 10^6$ (Ω cm K^{-1})	$A_{op} \times 10^6$ (Ω cm K^{-1})
0.1	253	33.39	56.03	53.64	24.8	89	209
0.125	274	37.17	61.88	59.70	18.4	93	70
0.15	283	40.13	66.37	64.33	14.2	120	13

sented in Table 4. We must mention that these computed values of ω_D, ω_{LO} and ω_{TO} for $La_{1-x}Na_xMnO_{3+y}$ with ($x = 0.1$, 0.125 and 0.15) could not be compared due to the lack of the experimental data. However, the computed values of Debye and Einstein temperature for $La_{0.7}Ba_{0.3}MnO_3$ manganite following the EIoIP approach yield consistent results with the available experimental results [22].

Fig. 4 illustrates the results of temperature dependence of resistivity in the metallic region via the electron–phonon interaction from Eq. (6). The residual resistivity ρ_0 and the coefficients A_{ac}, A_{op} as functions of doping concentration are shown in Table 4. It is noticed from the plot that the estimated ρ is lower than the reported data from $T \cong 125$ K to near the metal–insulator transition temperature (T_{mi}). The difference between the measured ρ and calculated ρ_{diff} [$=\rho_{\text{exp}} - \{\rho_0 + \rho_{\text{e-ph}}(=\rho_{ac} + \rho_{op})\}$] is plotted in Fig. 5. A quadratic temperature dependence of ρ_{diff} is depicted at low temperature. The quadratic temperature contribution for resistivity is an indication of conventional inelastic electron–electron scattering.

The quadratic temperature dependence of ρ_{diff} is consistent with the earlier argument made by Urushibara et al. [23]. The additional term due to electron–electron contribution was required in understanding the resistivity behavior, as extensive attempts to fit the data with residual resistivity and phonon resistivity were unsuccessful. It is noteworthy to comment that in conventional metals, the electron–electron contribution to the resistivity can at best be seen only at very low temperatures, due to its small magnitude in comparison with the phonon contribution. The existence of quadratic temperature dependence of resistivity over a wide temperature interval permits one to believe that the electron–electron scattering is also significant in determining the resistivity in manganites.

We again refer to Fig. 5, where a substantial deviation from the T^2-like behavior and a rapid rise in ρ_{diff} is observed in the intermediate temperature region ($175 < T < T_{mi}$). We perform the similar set of exercises with the difference between the measured ρ and calculated ρ_{diff} [$=\rho_{\text{exp}} - \{\rho_0 + \rho_{\text{e-ph}}(=\rho_{ac} + \rho_{op})\}$] beyond 175 K (plotted in Fig. 6). A $T^{4.5}$ temperature dependence of ρ_{diff} is depicted at higher temperature. The $T^{4.5}$ temperature contribution for resistivity is an indication of electron–magnon scattering. In the intermediate temperature region ($175 < T < T_{mi}$), the manganites appear to be normal metallic ferromagnet with the resistivity dominated by spin wave scattering. It is worth referring to an earlier work of Fulde and Jensen [24], who have argued that carrier density also changes by interaction with spin wave in manganites. The feature of $T^{4.5}$ temperature dependence of ρ_{diff} is consistent with the quantum theory of two-magnon scattering [25] and is valid for half-metallic ferromagnets.

Consequently, besides electron–phonon and electron–electron interaction, another explanation for the variation in carrier density is the presence of spin wave in the metallic system, and is caused by

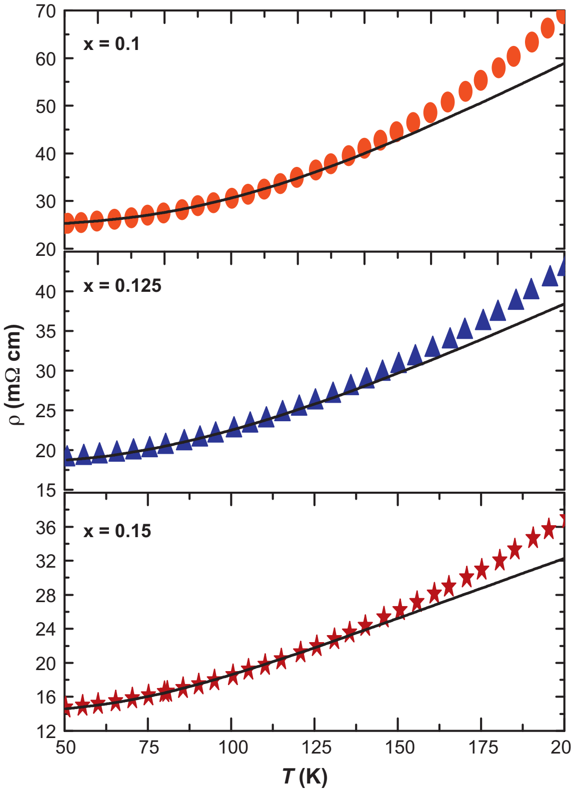

Fig. 4. Temperature dependence of the resistivity for $La_{1-x}Na_xMnO_{3+y}$ ($x = 0.1$, 0.125 and 0.15) samples in the metallic region. The solid lines are the best fits to Eq. (6).

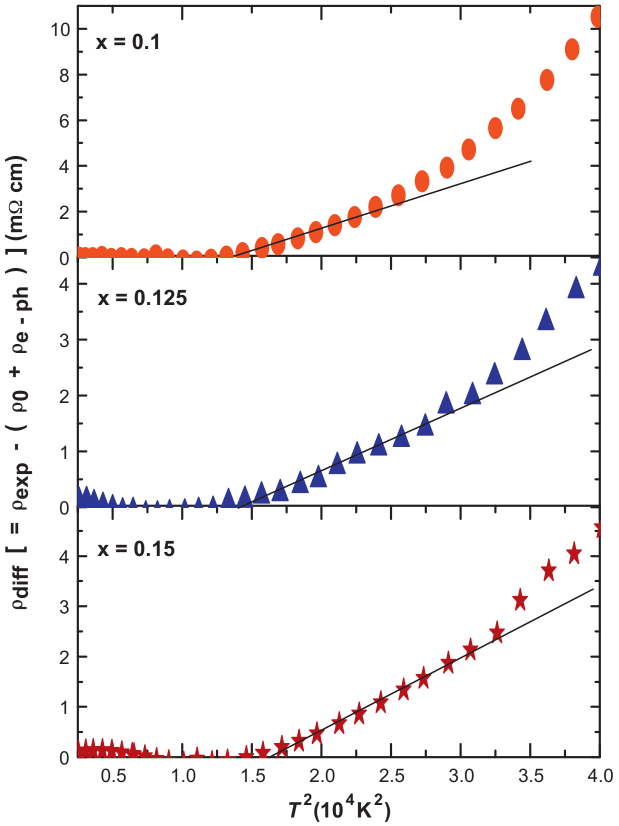

Fig. 5. Variation of ρ_{diff} [$=\rho_{\text{exp}} - \{\rho_0 + \rho_{\text{e-ph}}(=\rho_{ac} + \rho_{op})\}$] with T^2 for $La_{1-x}Na_xMnO_{3+y}$ ($x = 0.1$, 0.125 and 0.15) samples.

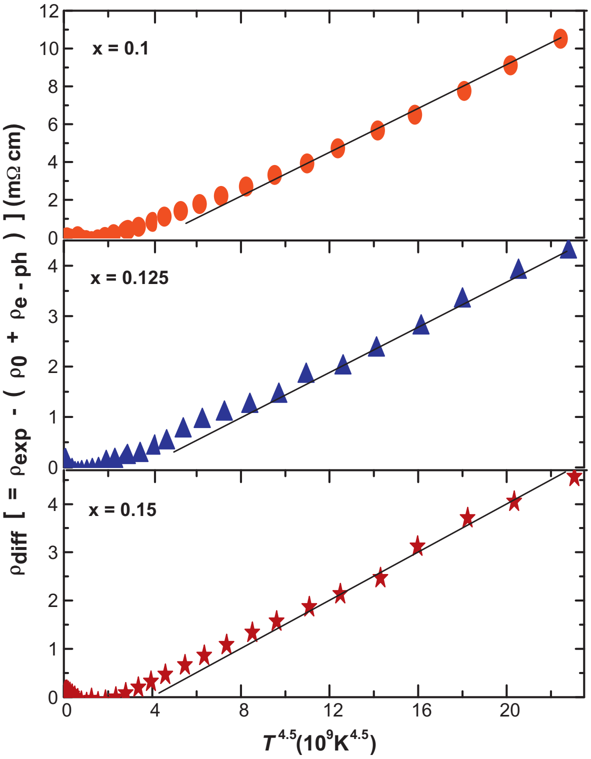

Fig. 6. Variation of ρ_{diff} [$=\rho_{\text{exp}}-\{\rho_0+\rho_{\text{e-ph}}(=\rho_{ac}+\rho_{op})\}$] with $T^{4.5}$ for $La_{1-x}Na_xMnO_{3+y}$ ($x=0.1$, 0.125 and 0.15) samples.

spin wave scattering. We finish by stating that the proposed model calculations reproduce the reported electrical behavior with a combination of $T^2$and $T^{4.5}$ apart from electron–phonon contribution, consistent with earlier predictions [26].

We now address the metallic behavior of doped manganites. If the high-frequency phonon modes are indeed strongly coupling with charge carriers, the effective mass of the carriers should be substantially enhanced. The Fermi energy and the corresponding density of states are conveniently obtained from the thermoelectric power results [27] using $\varepsilon_F=-\pi^2{k_B}^2T/[3|e|\ S_c^{\text{diff}}(T)]$ and $N(\varepsilon_F)=3n_{3D}V/2\varepsilon_F$ (where n_{3D} is the three-dimensional charge carrier density which is obtained following $n_{3D}d^3=1$ and V is the unit cell volume). The density of states in turn yields the electronic specific heat coefficient using $\gamma=(\pi k_B)^2N(\varepsilon_F)/3$ (see Table 5). It is noticed that the above values are consistent with the γ values in other hole doped divalent manganites [28] and could not be compared due to the lack of experimental data on hole doped monovalent manganites. The effective mass of the carrier along the conducting Mn–O plane is deduced from electronic specific heat coefficient γ, using, $m^*=3\hbar^2\pi\gamma d/{k_B}^2$.

The estimated electron parameters for $La_{1-x}Na_xMnO_{3+y}$ with $x=0.1$, 0.125, 0.15 are the Fermi wave vector k_F, the Fermi velocity v_F and the plasma frequency ω_p are given in the Table 5. We stress that the effects induced by electron correlations and mass renormalizations by electron–electron interactions are crucial in magnetic systems such as doped manganites [29].

It is known that in conventional metals, electron–phonon scattering is mathematically identical to conventional impurity scattering, and leads to a resistivity proportional to $({v_F}^2\ell)^{-1}$ where ℓ is the mean free path. The mean free path in this approximation is usually related to the Fermi velocity and is estimated following $\ell=v_F\tau$. We follow the Drude relation, $\tau^{-1}=\rho_0{\omega_p}^2/4\pi$, to obtain the scattering rate $R_s=\tau^{-1}$. The estimated values of R_s and ℓ are given in Table 5. We must mention that the residual resistance obtained for nominally the same compositions may vary significantly for different groups of compounds. It remains unclear whether ρ_0 only characterizes the sample's quality or if there is an intrinsic component in the residual resistivity [30]. For the Sr doped manganites, the resistivity data in the crystalline films yields ρ_0 as low as 10^{-5} Ω cm and is in the range of typical metallic conductors [23]. The deduced values of Fermi energy (ε_F) for $La_{1-x}Na_xMnO_{3+y}$ with $x=0.1$, 0.125, 0.15 corresponds to narrow energy band. We notice that the Na doped lanthanum manganites are good metals as the product $\varepsilon_F\tau>1$.

The electron correlations in view of mass enhancement effect in narrow band materials are important in doped $LaMnO_3$. We notice that enhanced electron mass $m^*/m_e>1$ in $La_{1-x}Na_xMnO_{3+y}$ (see Table 5), leads to the reduced plasma frequency, and hence the reduced zero temperature elastic scattering rate in comparison to conventional metals. It is perhaps worth noticing that, in hole-doped manganites, the scattering rate at low temperatures is of the order of 10^{15} s^{-1} [25]. Furthermore, the Mott–Ioffe–Regel criterion for metallic conductivity is valid, as the deduced mean free path is greater than the Mn–O bond length. The use of the Bloch–Gruneisen expression in estimating the electron–phonon contributions is thus validated as the product $k_F\ell\sim1$.

The monovalent Na doped manganites thus illustrate a metallic behavior below metal–insulator transition temperature T_{mi}. The T_{mi} increases with the Na doping concentration. With increased doping, the monovalent Na doped manganites behaves as good metal and is attributed to the fact that there are twice as many Mn^{4+} ions as there are Na ions and each of these Mn^{4+} will contribute a hopping hole.

We must refer to the work of Egilmez and researchers who incorporate the effects of the grain-boundary-induced lattice disorder on the resistivity in $Sm_{0.55}Sr_{0.45}MnO_3$ at temperatures near the metal–insulator transition [31]. The low temperature resistivity data ($T\leq75$ K) of the SmSrMnO was successfully fitted using the relation $\rho=\rho_0+\rho_2T^2+\rho_5T^5$ with ρ_0 as the residual resistivity and ρ_2 and ρ_5 are the electron–electron and the electron–phonon scattering coefficients, respectively. It is further noticed that in this temperature range, the disorder does not affect the temperature dependence of ρ however; it causes an increase in the coefficients ρ_0, ρ_2 and ρ_5 by two orders of magnitude.

In contrast to electron–phonon scattering as the source of resistivity in ferromagnetic metallic (FM) state, the angle-resolved photoemission spectroscopy data for the bilayer manganite $La_{1.2}Sr_{1.8}Mn_2O_7$ identifies a coherent polaronic metallic ground state below metal–insulator transition [32]. The FM state is a polaronic metal with a strong anisotropic character of the electronic excitations, strikingly similar to the pseudogap phases in heavily underdoped cuprate high temperature superconductors as Bi 2212. A strong mass enhancement and a small renormalization factor are found to account for the metallic properties [33]. The temperature

Table 5
The estimated electron parameters for $La_{1-x}Na_xMnO_{3+y}$ ($x=0.1$, 0.125, 0.15) manganites.

x	ε_F (eV)	$N(\varepsilon_F)\times10^{-19}$ (eV^{-1} cm^{-3})	γ (mJ mol^{-1} K^{-2})	m^*/m_e	$k_F\times10^{-7}$ (cm^{-1})	$v_F\times10^{-7}$ (cm s^{-1})	ω_p (eV)	$R_s\times10^{-14}$ (s^{-1})	ℓ (Å)
0.1	1.649	2.893	2.533	1.391	3.759	3.119	1.827	16.92	1.843
0.125	0.825	5.775	5.056	2.776	3.759	1.563	1.294	6.274	2.491
0.15	0.6	7.919	6.933	3.804	3.762	1.141	1.106	3.563	3.203

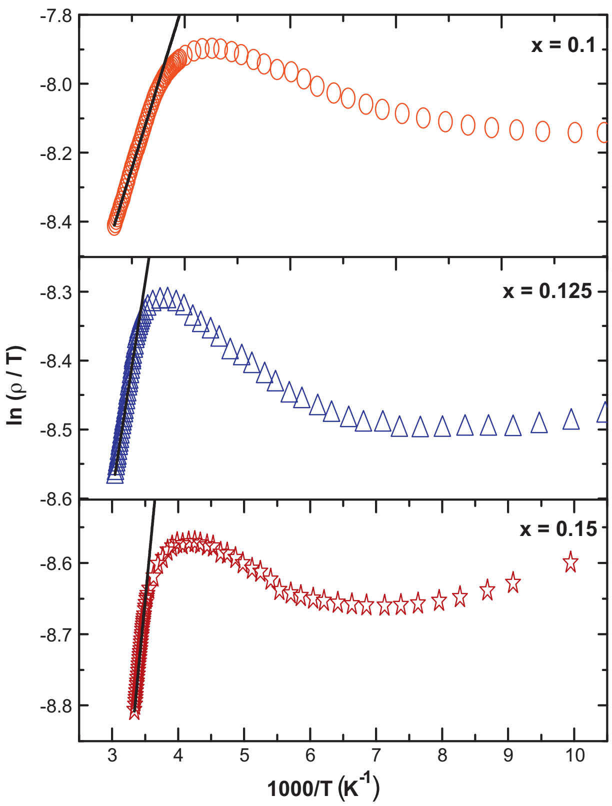

Fig. 7. Variation of $\ln(\rho/T)$ with $1000/T$ for $La_{1-x}Na_xMnO_{3+y}$ ($x = 0.1$, 0.125 and 0.15) samples in high temperature region, $T > T_{mi}$. The solid line shows fitting to the equation $\rho = \rho_{os}T\exp(E_p/k_BT)$.

Table 6
Parameters obtained corresponding to the best fit to the experimental data of $La_{1-x}Na_xMnO_{3+y}$ samples by using SPC model.

x	$n \times 10^{-21}$ (cm^{-3})	$\rho_{os} \times 10^6$ (Ω cm K^{-1})	E_p (meV)
0.1	2.731	8.313	85.01
0.125	2.885	7.292	84.13
0.15	3.381	5.965	83.14

dependence of resistivity in the metallic state is intimately related to polaronic metallic ground state and the insulator-to-metallic state can be attributed to polaron coherence condensation process acting in concert with the Double exchange mechanism. We may comment that the present theory finds an enhanced mass of holes as carrier ($m^*/m_e > 1$ for $La_{1-x}Na_xMnO_{3+y}$ with $x = 0.1$, 0.125, 0.15) from the electronic specific heat coefficient to validate the Mott–Ioffe–Regel criterion. However, a detailed analysis is further required to understand the polaronic metallic state in the ferromagnetic phase and the condensation process analogous to underdoped cuprate high temperature superconductors. We shall address this issue in near future.

We have further analyzed the resistivity data of high temperature region, $T > T_{mi}$, using adiabatic small polaron conduction (SPC) model. Above the metal–insulator transition temperature (T_{mi}), the Jahn–Teller-type distortion present in the unit cell traps the charge carriers and gives rise to polarons. We must mention that the most rapid motion of a small polaron occurs when the carrier hops each time the configuration of vibrating atoms in an adjacent site coincides with that in the occupied site. Henceforth, the charge carrier motion within the adiabatic regime is faster than the lattice vibrations and the resistivity for SPC follows $\rho = \rho_{os}T\exp(E_p/k_BT)$ with the polaron formation energy E_p and Boltzman constant k_B [34]. In the above expression $\rho_{os} = k_B/n(1-x)e^2D$, where n is the charge carrier density, x is the doping fraction, e is the electronic charge, and D is the polaron diffusion constant ($D = a^2\nu/6$ for a typical cubic coordination where a is being the lattice constant and ν, the characteristic frequency of the longitudinal optical phonon that carries the polaron through the lattice). The fitted curves are shown by thick solid lines in Fig. 7 and the fitting parameters are given in Table 6. As expected, the charge carrier density (n) increases with increasing Na concentration in $La_{1-x}Na_xMnO_{3+y}$, which confirms that the observed decrease in resistivity is due to the systematic increase of charge carriers with monovalent substitution.

As discussed earlier, the resistivity of all the samples shows an upturn at some T_{min} (see Fig. 8). In order to understand the origin of the observed resistivity minimum in manganites, the experimental data had been analyzed taking account of Kondo-like scattering, the electron–electron interaction, weak localization, intergranular tunneling of the polarized charge carriers, and so on [18–21,35]. We may refer to Tiwari and coworkers [18] who explain the low-temperature electrical resistivity minimum observed in $La_{0.7}A_{0.3}MnO_3$, (A = Ca, Sr, Ba) perovskite oxides in terms of a $T^{1/2}$ dependence of conductivity, which is a characteristic of 3D disordered metallic systems with enhanced electron–electron interactions due to disorder. The origin of such unusual contribution has been attributed to Coulomb interaction (CI) between carriers strongly enhanced by disorder [36] inherent in ceramic system. However, Xu et al. [21] argued that along with the electron–electron interactions Kondo-like spin dependent scattering should also contribute to the resistivity minimum for polycrystalline $La_{2/3}Ca_{1/3}MnO_3$ sample for lower fields ($H < 1.0$ T).

The resistivity minimum at low temperatures comes from the competition of two contributions: one, usually, increases and the other, decreases with the increase of the temperature. It is well known that the resistivity come from the electron–phonon

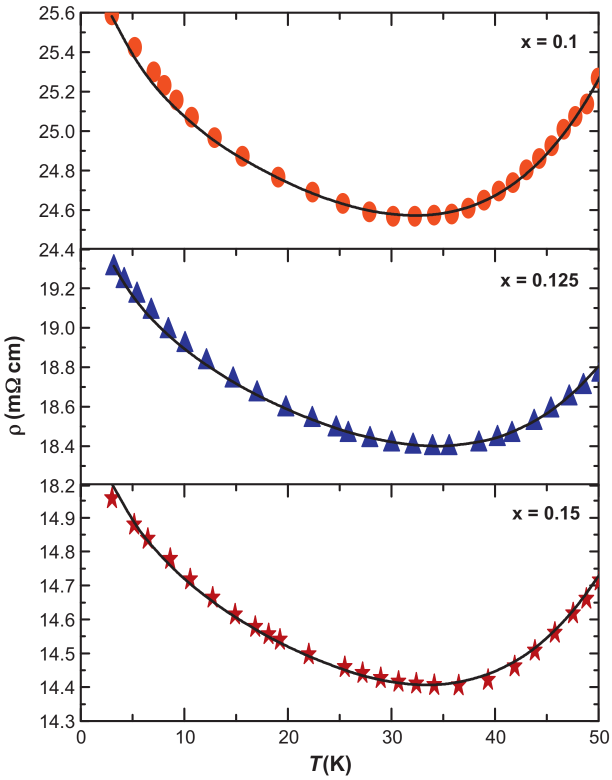

Fig. 8. Temperature dependence of the resistivity for $La_{1-x}Na_xMnO_{3+y}$ ($x = 0.1$, 0.125 and 0.15) samples below 50 K. All curves show an upturn with decrease in temperature. The solid lines are the best fits to Eq. (7).

Table 7
Parameters obtained corresponding to the best fit to the experimental data of $La_{1-x}Na_xMnO_{3+y}$ samples below 50 K.

x	σ_0 (Ω^{-1} cm^{-1})	σ_e (Ω^{-1} cm^{-1} K$^{-1/2}$)	$\rho_P \times 10^{12}$ (Ω cm K^{-5})	$\rho_S \times 10^4$ (Ω cm K^{-1})
0.1	38.32	0.18	3.5	2.8
0.125	50.51	0.35	2.4	2.1
0.15	65.36	0.42	1.8	1.2

interaction increases with the increase of temperature and the contributions from the electron–electron and the spin-disorder scattering decrease with the increase of temperature. Therefore, we fitted the low-temperature ($T < 50$ K) resistivity data to the expression

$$\rho(T) = \left[\frac{1}{\sigma_0 + \sigma_e\sqrt{T}}\right] - C \ln T + \rho_P(T)^5. \qquad (7)$$

Here in the first term σ_0, the residual conductivity contributed by the temperature-independent scattering processes and the contribution of electron–electron scattering is considered together, the second term may reflect the Kondo-like spin dependent scattering and the third term corresponds to the electron–phonon interaction. The $\rho(T)$ data for all the samples for $T < 50$ K, are fitted to equation (7). Excellent fits are obtained as shown by the solid lines in Fig. 8. The coefficients of the fits are given in Table 7. Xu et al. [21] also reported fairly good agreement for the resistivity minimum in $La_{2/3}Ca_{1/3}MnO_3$ sample and had theoretically shown the typical expected nature of the resistivity minimum for fields ($H < 1.0$ T) by considering both the electron–electron interactions (attributed to CI) in terms of $T^{1/2}$ dependence and the Kondo-like spin dependent scattering in terms of ln T dependence.

4. Conclusions

In conclusion, the relationship between compositions of La^{3+} based manganites $La_{1-x}Na_xMnO_{3+y}$ for low doping Na^+ concentration (x = 0.1, 0.125, and 0.15) and structural as well as transport properties has been studied. XRD patterns indicate that all synthesized compounds posse's rhombohedral structure with space group $R\bar{3}C$. The unit-cell volume decreases and tolerance factor t increases with enhanced Na doping due to increase Mn^{4+} content. Enhanced Na content leaves an increased number of holes in the Mn e_g band, hence there are effectively more charge carriers leading to enhance hopping interaction and results in increased conductivity.

The electrical resistivity of all the samples shows metal–insulator transition at transition temperature T_{mi}. It is clearly seen that T_{mi} increases gradually with increased dopant concentration in $La_{1-x}Na_xMnO_{3+y}$. The metallic behavior of resistivity in the temperature range ($50 \le T \le T_{mi}$) is retraced by using electron–phonon interaction with the model phonon spectrum comprising of an acoustic branch of Debye type and optical mode with characteristic Einstein temperature. The contribution from acoustic and optical phonons together with the residual resistivity is smaller than experimental data. A clear straight line is depicted from ~140 K to ~175 K temperature range while plotting the difference as a function of T^2 indicative of electron–electron scattering. We further explore the role of electron–magnon scattering in the electrical transport mechanism. It is noticeable that the role of two-magnon scattering in the resistivity behavior is prominent above 175 K. The incorporation of $T^{4.5}$ dependence is essential and consistently retraces the measured resistivity at higher temperatures. It is inferred from the above analysis that the electrical transport below T_{mi} is not only dominated by electron–electron scattering, but also by electron–magnon, presumably involving spin fluctuations of charge carriers.

The resistivity data of semiconducting state at high temperature region, $T > T_{mi}$, is analysed by using adiabatic small polaron conduction (SPC) model. The nearest-neighbour hopping of a small polaron leads to a mobility with a thermally activated form and successfully retraced the reported experimental curve in the paramagnetic phase. The E_p gradually decreases with doping and is due to phonon softening effect on carrier transport owing to Jahn-Teller distortions in the $La_{1-x}Na_xMnO_3$. Above T_{mi} the Jahn-Teller-type distortion present in the unit cell traps the charge carriers and gives rise to polarons. Hence above T_{mi} the resistivity shows a polaronic-type behavior. In the ferromagnetic region, along with metallic conductivity, at low temperature (below 50 K) a resistivity upturn is observed along with a $T^{1/2}$ and ln T dependence of the resistivity, which indicates that the resistivity upturn are due to contribution of CI and Kondo-like spin dependent scattering.

Conclusively, we have made an attempt to measure and also analyse the electrical resistivity behavior in Na doped manganites based on CI and Kondo-like spin dependent scattering (below 50 K), electron–phonon, electron–electron and electron–magnon scattering in the metallic region ($T \le T_{mi}$), and small polaron conduction ($T > T_{mi}$). The scheme opted in the present study is so natural that it extracts only the essential contributions to describe the resistivity behavior. Although we have provided a simple explanation of these effects, there is a clear need for good theoretical understanding of the resistivity behavior in view of the formation of small polarons may be of magnetic origin in manganites.

Acknowledgements

Authors are thankful to UGC-DAE CSR, Indore for providing characterization facilities. Useful discussions with Dr. R. Rawat are gratefully acknowledged. One of us (M.W.S.) is gratefully acknowledged for the award of Senior research fellowship from Council of Scientific and Industrial Research, New Delhi, India. Financial assistance from MPCST, Bhopal, India is gratefully acknowledged.

Appendix A. Appendix

The understanding of the dynamical properties of materials requires the formulation of an effective interionic potential. This is particularly important, as there is much disagreement as to whether long- or short-range interactions are at the origin of the substantial properties manganites. To begin with, we made the following assumptions: the change in force constants is small; the short-range interactions are effective up to the second-neighbour ions; and the atoms are held together by harmonic elastic forces without any internal strains within the crystal. We thus express the crystal energy for a particular lattice separation (r) as:

$$U(r) = U_C(r) + U_R(r) + U_V(r). \qquad (A1)$$

The first term is the Coulomb energy, and follows:

$$U_C(r) = -\sum_{ij} \frac{Z_i Z_j e^2}{r_{ij}} = -\frac{\alpha_m Z^2 e^2}{r}, \qquad (A2)$$

with α_m as the Madelung constant [37] and r_{ij} being the separation distance between i and j ions.

The short-range overlap repulsive energy is the second term in Eq. (A1), and is expressed as:

$$U_R(r) = nb\beta_{ij}\ \exp\left(\frac{r_i + r_j + r_{ij}}{\rho}\right) + n'b\beta_{ij}\ \exp\left(\frac{2r_i - kr_{ij}}{\rho}\right) + n'b\beta\ \exp\left(\frac{2r_j - kr_{ij}}{\rho}\right), \tag{A3}$$

following Hafemeister and Flygare [38]. The ionic radii are r_i and r_j, k is the structure factor, $n(n')$ is the number of nearest (next nearest) ions, respectively. Further, the notations b and ρ denote the hardness and range parameters, respectively.

The Pauling coefficients, β_{ij} are defined in terms of valency [Z_i (Z_j)] and number of the outermost electrons [n_i (n_j)] in the anions (cations) respectively as:

$$\beta_{ij} = 1 + \left(\frac{z_i}{n_j}\right) + \left(\frac{z_j}{n_j}\right). \tag{A4}$$

The last term in Eq. (A1) is the van der Waals (vdW) energy, denoted as:

$$U_V(r) = -\left(\sum_{ij}\frac{C_{ij}}{r_{ij}^6} + \sum_{ij}\frac{d_{ij}}{r_{ij}^8}\right), \tag{A5}$$

$$= \left(\frac{C}{r^6} + \frac{D}{r^8}\right), \tag{A6}$$

due to dipole–dipole (d–d) and dipole–quadruple (d–q) interactions. The abbreviations C and D represent the overall vdW coefficients, defined as [37]:

$$C = c_{ij}S_6(r) + \frac{1}{2}(c_{ii} + c_{jj})S_6(0), \tag{A7}$$

and

$$D = d_{ij}S_8(r) + \frac{1}{2}(d_{ii} + d_{jj})S_8(0), \tag{A8}$$

c_{ij} and d_{ij} are the vdW coefficients due to d–d and d–q interactions. We follow the variational method [39] to derive c_{ij} and d_{ij} as:

$$C_{ij} = \frac{3}{2}\frac{e\hbar}{\sqrt{me}}\alpha_i\alpha_j\left[\left(\frac{\alpha_i}{N_i}\right)^{1/2} + \left(\frac{\alpha_j}{N_j}\right)^{1/2}\right]^{-1}, \tag{A9}$$

and

$$d_{ij} = \frac{27}{8}\frac{\hbar^2}{m}\alpha_i\alpha_j\left[\left(\frac{\alpha_i}{N_i}\right)^{1/2} + \left(\frac{\alpha_j}{N_j}\right)^{1/2}\right]^2\left[\frac{\alpha_i}{N_i} + \frac{20}{3}\left(\frac{\alpha_i\alpha_j}{N_iN_j}\right)^{1/2} + \frac{\alpha_j}{N_j}\right]^{-1}. \tag{A10}$$

Here, m_e is the electron mass, α_i is the electronic polarisability and N_i denotes the effective number of electrons of the ith ion. The values of the overall vdW coefficients are obtained using Eqs. (A7)–(A10), and weighted in terms of appropriate lattice sums [$S_6(0)$, $S_6(r)$, $S_8(0)$ and $S_8(r)$] [37]. We believe that there is no uncertainty involved in the evaluation of c_{ij} and d_{ij}, due to the fact that the excitation energies are ignored in Eqs. (A9) and (A10). Herein, the above description we shall seek the interionic interaction in between a pair such as Mn–O and La/Na–O.

It is clear from the above descriptions that the present effective interionic potential contains only two free parameters (range b and hardness ρ), which are determined from the equilibrium conditions:

$$\left(\frac{dU}{dr}\right)_{r=r_0} = 0, \tag{A11}$$

and bulk modulus

$$B_T = \frac{1}{9kr_0}\left(\frac{d^2U}{dr^2}\right)_{r=r_0}. \tag{A12}$$

While estimating these values, we used the input parameters B_T [40] and r_0 (obtained from Rietveld refinement of XRD data). The model parameters obtained from Eqs. (A11) and (A12) have been used to compute the second order elastic constants (C_{11}, C_{12} and C_{44}) as [41]

$$C_{11} = \frac{e^2}{4r_0^4}\left[-5.112Z_m^2 + A_1 + \frac{A_2 + B_2}{2}\right], \tag{A13}$$

$$C_{12} = \frac{e^2}{4r_0^4}\left[0.226Z_m^2 + B_1 + \frac{A_2 + 5B_2}{2}\right], \tag{A14}$$

$$C_{44} = \frac{e^2}{4r_0^4}\left[2.556Z_m^2 + B_1 + \frac{A_2 + 3B_2}{2}\right], \tag{A15}$$

where (A_1, B_1) and (A_2, B_2) are the short-range parameters for the nearest and the next nearest neighbours, respectively. These parameters are defined as

$$A_1 = \frac{4r_0^3}{e^2}\left[\frac{d^2}{dr^2}V_{ij}(r)\right]_{r=r_0}, \tag{A16}$$

$$A_2 = \frac{4(r_0\sqrt{2})^3}{e^2}\left[\frac{d^2}{dr^2}V_{ii}(r) + \frac{d^2}{dr^2}V_{jj}(r)\right]_{r=r_0\sqrt{2}}, \tag{A17}$$

$$B_1 = \frac{4r_0^3}{e^2}\left[\frac{d}{dr}V_{ij}(r)\right]_{r=r_0}, \tag{A18}$$

$$B_2 = \frac{4(r_0\sqrt{2})^2}{e^2}\left[\frac{d}{dr}V_{ii}(r) + \frac{d}{dr}V_{jj}(r)\right]_{r=r_0\sqrt{2}}, \tag{A19}$$

where $V_{ij}(r)$ is the short-range potentials between the ions, which follow

$$V_{ij}(r) = b\beta_{ij}\ \exp\left(\frac{r_i + r_j - r_{ij}}{\rho}\right) + C_{ij}r_{ij}^{-6} + d_{ij}r_{ij}^{-8}. \tag{A20}$$

The elastic force constant κ is derived at the equilibrium interionic distance r_0 following

$$\kappa = \frac{r_0}{2}[\pi^2(C_{11} - C_{12})(C_{11} + C_{12} + 2C_{44})(C_{44})]^{1/3}. \tag{A21}$$

We have thus estimated the elastic force constants in terms of the developed EIoIP for a pair such as Mn–O and La/Na–O and have the total of the Na doped $LaMnO_3$. This continuum model thus takes care of the clear physical binding in doped manganites. We stress that the simple models based on this potential can describe those cohesive properties of such solids that depend on van der Waals interactions. However, the true potential must recognize the correct charge distribution and the relative orientations of the interacting atoms in manganites which is a complicated task.

We shall now estimate the acoustic Debye branch characterized by the Debye temperature θ_D and an optical peak defined by the Einstein temperature θ_E. The Debye frequency is characterized as a cut off frequency at the Brillouin zone boundary. It can be expressed in terms of effective value of ionic mass and elastic force constant for crystal lattices with two different kinds of atoms such as Mn–O and La/Na–O, which we deal with. The acoustic-mode and optical-mode frequencies are estimated in an ionic model using a value of effective ion charge $Ze = -2e$.

We choose an acoustic mass $M = (2M_+ + M_-)$ [Mn (O) which is symbolized by $M_+(M_-)$], $\kappa^* = 2\kappa$ for each directional oscillation mode to get the acoustic phonon frequency as [26]

$$\omega_D = \sqrt{\frac{2\kappa^*}{M}}. \tag{A22}$$

Furthermore, when the phonons belong to optic modes, their frequency is determined by the reduced mass as

$\mu^{-1} = M(\mathrm{A})^{-1} + M(\mathrm{B})^{-1}$ where A is the anion (La/K, Mn) and B is the cation (O)

$$\omega_{LO}^2 = \frac{\kappa + \eta}{\mu}, \tag{23}$$

$$\omega_{TO}^2 = \frac{\kappa - \eta}{\mu}, \tag{24}$$

where η is the force constant as

$$\eta = \frac{8\pi}{3}\frac{(Ze)^2}{\Omega}, \tag{25}$$

ω_{LO} (ω_{TO}) symbolized for the longitudinal (transverse) optical phonon frequency and Ω for the volume of the unit cell.

It is true that the two-orbital model based on Wannier functions predicts the electronic states such as charge ordering in manganites. It is pointed out by Marzari et al. that the Wannier function approach of the electronic problem is useful for the description of electron dynamics following semi-classical theory as well as the magnetic interactions in solids [42]. In the present investigations, we do not intended to discuss the electron dynamics as well the magnetic interactions, but focused on determining the acoustic (optical) phonon frequency to estimate the electron–phonon contribution of resistivity in the ferromagnetic metallic phase.

The developed effective interionic interaction potential takes care of the interactions in between a pair such as Mn–O and La/Na–O. The interactions thus are attractive Coulomb, and van der Waals (vdW) as well as short-range overlap repulsive interaction following Hafemeister and Flygare type potential. The advantage of using this potential is that it takes care of number of nearest (next nearest) ions, the valency, and number of the outermost electrons in the anions (cations), respectively. Thus it takes care of the structural parameters that yield an approximately correct description of the interactions between a pair such as Mn–O and La/Na–O. Henceforth; we are able to estimate the acoustic (optical) phonon frequency consistent with the Raman measurements to estimate the electron–phonon contribution of resistivity.

We must refer to the work of Millis [43] who determines the elastic parameters using a mean field approximation with emphasis on Mn–O bond lengths and evaluated Mn-Mn and Mn–O force constants for the lattice distortions. On the other hand, in the present model we have considered both Mn–O and La/Na–O bond lengths to obtain the Mn–O, La/Na–O and total force constants for strong electron–phonon interaction. The formulated effective interionic interaction potential includes the long-range Coulomb, van der Waals (vdW) interaction and the short-range repulsive interaction up to second neighbour ions within the Hafemeister and Flygare approach. The interionic interaction in between a pair such as Mn–O and La/Na–O enable us to find the total force constant with consistent Debye and Einstein temperatures.

References

[1] T. Sarkar, B. Ghosh, A.K. Raychaudhuri, Phys. Rev. B 77 (2008) 235112.
[2] S.V. Trukhanov, L.S. Lobanovski, M.V. Bushinsky, I.O. Troyanchuk, H. Szymczak, J. Phys. Condens. Matter 15 (2003) 1783.
[3] A.K. Saket Asthana, S.K. Nigam, D. Malik, Bahadur, J. Alloys Compd. 450 (2008) 136.
[4] C.C. Chen, C.H. Shen, R.S. Liu, J.G. Lin, C.Y. Huang, Mater. Res. Bull. 37 (2002) 235.
[5] R.J.H. Voorhoeve, J.P. Remeika, L.F. Trimble, A.S. Cooper, F.J. Disalvo, P.K. Gallagher, Solid State Chem. 14 (1975) 395.
[6] (a) M. Itoh, T. Shimura, J.D. Yu, T. Hayashi, Y. Inaguma, Phys. Rev. B 52 (1995) 12522;
(b) A.I. Tovstolytkin, V.M. Tsmots, L.I. Pankiv, P.G. Litovchenko, I.S. Pankiv, Low Temp. Phys. 36 (2010) 220.
[7] (a) G.H. Rao, J.R. Sun, K. Barner, N. Hamad, J. Phys. Condens. Matter 11 (1999) 1523;
(b) A.M. Aliev, A.G. Gamzatov, A.B. Batdalov, A.S. Mankevich, I.E. Korsakov, Physica B 406 (2011) 885.
[8] (a) C. Boudaya, L. Laroussi, E. Dhahri, J.C. Joubert, A. Cheikh-Rouhou, J. Phys. Condens. Matter 10 (1998) 7485;
(b) M. Koubaa, Y. Regaieg, W. CheikhrouhouKoubaa, A. Cheikhrouhou, S. Ammar-Merah, F. Herbst, J. Magn. Magn. Mater. 323 (2011) 252.
[9] C. Zener, Phys. Rev. 82 (1951) 403.
[10] A.J. Millis, P.B. Littlewood, B.I. Shraiman, Phys. Rev. Lett. 74 (1995) 5144.
[11] H.Y. Hwang, S.-W. Cheong, P.G. Radaelli, M. Marezio, B. Batlogg, Phys. Rev. Lett. 75 (1995) 914.
[12] X.J. Fan, J.H. Zhang, X.G. Li, W.B. Wu, J.Y. Wan, T.J. Lee, H.C. Ku, J. Phys. Condens. Matter 11 (1999) 3141.
[13] J. Töpfer, J.B. Goodenough, J. Solid State Chem. 130 (1997) 117.
[14] N. Abdelmoula, K. Guidara, A. Cheikhrouhou, E. Dhahri, J.C. Joubert, J. Solid State Chem. 151 (2000) 139.
[15] J. Rodriguez-Carvajal, FULLPROF version 3.0.0, Laboratorie Leon Brillioun, CEA–CNRS, 1995.
[16] S. Roy, Y.Q. Guo, S. Venkatesh, N. Ali, J. Phys. Condens. Matter 13 (2001) 9547.
[17] R.D. Shannon, Acta Cryst. A 32 (1976) 751.
[18] A. Tiwari, K.P. Rajeev, Solid State Commun. 111 (1999) 33.
[19] M. Ziese, Phys. Rev. B 68 (2003) 132411.
[20] D. Kumar, J. Sankar, J. Narayan, R.K. Singh, A.K. Majumdar, Phys. Rev. B 65 (2002) 094407.
[21] Y. Xu, J. Zhang, G. Cao, C. Jing, S. Cao, Phys. Rev. B 73 (2006) 224410.
[22] D. Varshney, M.W. Shaikh, I. Mansuri, J. Alloys Compd. 486 (2009) 726.
[23] A. Urushibara, Y. Moritomo, T. Arima, A. Asamitsu, G. Kido, Y. Tokura, Phys. Rev. B 51 (1995) 14103.
[24] P. Fulde, J. Jensen, Phys. Rev. B 27 (1983) 4085.
[25] K. Kubo, N. Ohata, J. Phys. Soc. Jpn. 33 (1972) 21.
[26] (a) D. Varshney, N. Kaurav, Eur. Phys. J. B 40 (2004) 129;
(b) D. Varshney, N. Kaurav, J. Low Temp. Phys. 141 (2005) 315.
[27] T. Shimura, T. Hayashi, Y. Inaguma, M. Itoh, J. Solid State Chem. 124 (1996) 250.
[28] L. Ghivelder, I.A. Castillo, McN.N. Alford, G.J. Tomka, P.C. Riedi, J. MacManus-Driscoll, A.K.M. Akther Hossain, L.F. Cohen, J. Magn. Magn. Mater. 189 (1998) 274.
[29] D. Varshney, N. Kaurav, Eur. Phys. J. B 37 (2004) 301.
[30] M. Quijada, J. Cerne, J.R. Simpson, H.D. Drew, K.H. Ahn, A.J. Millis, R. Shreekala, R. Ramesh, M. Rajeswari, T. Venkatesan, Phys. Rev. B 58 (1998) 16093.
[31] M. Egilmez, K.H. Chow, J. Jung, I.A. Fan, I. Mansour, Z. Salman, Appl. Phys. Lett. 92 (2008) 132505.
[32] N. Mannella, W.L. Yang, K. Tanaka, X.J. Zhou, H. Zheng, J.F. Mitchell, J. Zaanen, T.P. Devereaux, N. Nagaosa, Z. Hussain, Z.X. Shen, Phys. Rev. B 76 (2007) 233102.
[33] N. Mannella, W.L. Yang, X.J. Zhou, H. Zheng, J.F. Mitchell, J. Zaanen, T.P. Devereaux, N. Nagaosa, Z. Hussain, Z.X. Shen, Nature 438 (2005) 474.
[34] A.S. Alexandrov, N.F. Mott, Polarons and Bipolarons, World Scientific, Singapore, 1995;
G.J. Snyder, R. Hiskes, S. DiCarolis, M.R. Beasley, T.H. Geballe, Phys. Rev. B 53 (1996) 14434.
[35] M. Auslender, A.E. Kar'kin, E. Rozenberg, G. Gorodetsky, J. Appl. Phys. 89 (2001) 6639.
[36] P.A. Lee, T.V. Ramkrishnan, Rev. Mod. Phys. 57 (1985) 287.
[37] M.P. Tosi, Solid State Phys. 16 (1964) 1.
[38] D.W. Hafemeister, W.H. Flygare, J. Chem. Phys. 43 (1965) 795.
[39] J.C. Slater, J.G. Kirkwood, Phys. Rev. 37 (1931) 682.
[40] V. Markovich, I. Fita, R. Puzniak, E. Rozenberg, C. Martin, A. Wisniewski, A. Maignan, B. Raveau, Y. Yuzhelevskii, G. Gorodetsky, Phys. Rev. B 70 (2004) 024403.
[41] (a) D. Varshney, N. Kaurav, R. Kinge, R.K. Singh, J. Phys. Condens. Matter 19 (2007) 236204;
(b) D. Varshney, U. Sharma, N. Kaurav, J. Phys. Condens. Matter 20 (2008) 075204.
[42] N. Marzari, D. Vanderbilti, Phys. Rev. B 56 (1997) 12847.
[43] A.J. Millis, Phys. Rev. B 53 (1996) 8434.